

# **Beyond KOH activation for the synthesis of superactivated carbons from hydrochar**

**Marta Sevilla,\* Guillermo A. Ferrero, Antonio B. Fuertes**

*Instituto Nacional del Carbón (CSIC), P.O. Box 73, Oviedo 33080, Spain*

\*Corresponding author: [martasev@incar.csic.es](mailto:martasev@incar.csic.es)

## Abstract

A novel activating agent for the production of highly microporous carbons with textural properties that match those of superactivated carbons prepared by KOH activation, *i.e.* BET surface areas of 2600-3000 m<sup>2</sup> g<sup>-1</sup>, pore volumes of ~1.3-1.6 cm<sup>3</sup> g<sup>-1</sup> and pore size distributions in the supermicropore-small mesopore (< 3 nm) region, is studied. It consists of a mixture of melamine and potassium oxalate, a substance which is less corrosive than KOH, imposing less technical restrictions. Additional advantages of this activating agent are that the morphology of the particles is not altered and, importantly, the product yield is almost double that of KOH activation. The advantageous textural characteristics of the produced materials are combined with a relatively good electronic conductivity of ~2-3 S cm<sup>-1</sup>. When tested as supercapacitor electrodes using conventional electrolytes such as H<sub>2</sub>SO<sub>4</sub> and TEABF<sub>4</sub>/AN, and less conventional ones such as EMImTFSI/AN, these carbons match the performance of benchmark KOH activated carbons and surpass that of commercial activated carbons specifically designed for supercapacitor applications.

## 1. Introduction

Activated carbons (ACs) have a long history of success. The first recorded case dates back to 3750 BC, when the Egyptians and Sumerians used wood char for the reduction of copper, zinc and tin ores in the manufacture of bronze [1]. Later on, the Egyptians used it for medicinal purposes around 1550 BC [2]. Since then, ACs have been used in a wide range of applications, ranging from environmental remediation [3] to gas storage [4] and electrochemical energy storage [4, 5]. In particular, AC is used to assemble nearly all commercial supercapacitors owing to its high surface area, relatively low cost, good electronic conductivity, well-developed manufacturing technologies and easy production in large quantities. However, on the down side, current supercapacitor ACs have a limited porosity (surface area  $< 1800 \text{ m}^2 \text{ g}^{-1}$ ) which limits charge storage and a tortuous porosity which hinders the diffusion of ions, thereby hampering their power capability. Accordingly, current research efforts are directed towards the development of highly porous materials with textural and morphological properties that enhance ion storage and transport properties. To this end, chemical activation with KOH is being widely investigated as it allows the production of ACs with ultra-large surface areas ( $1500 - 3500 \text{ m}^2 \text{ g}^{-1}$ ) from a variety of precursors (coal, polymers, biomass or hydrothermally carbonized biomass, graphene, etc.) [4, 6]. Its large scale industrial implementation however is hindered by the high corrosiveness of KOH and its toxicity, with the result that the final product is expensive and only used in high-end applications. This has led some scientists to explore alternative chemical agents for the production of ACs with advanced and controlled properties.

Additionally, growing concern about sustainability has shifted attention towards the use of biomass or biomass derivatives as carbon precursors. For example, Fellingner's group has revisited  $\text{ZnCl}_2$  as chemical activating agent and used its low melting eutectic mixtures with several chloride salts (e.g. KCl, NaCl or LiCl) to produce hierarchical porous carbons (surface area up to ca.  $3000 \text{ m}^2 \text{ g}^{-1}$ ) by using firstly ionic liquids [7] and more recently adenine [8] and glucose [9] as carbon precursor. They have called this strategy "salt-templating" or "ionothermal carbonization". Other authors have combined multi-scale inorganic salts and by controlling their crystallization and assembly through a freeze-drying process, have been able to produce 3D porous carbon networks from glucose [10]. More recently, Deng *et al.* have followed a green "leavening" strategy, in which potassium bicarbonate leads to materials with a 3D hierarchical pore structure when mono-, polysaccharides and biomass are used as carbon precursors [11]. However, when hydrochar is the carbon precursor, potassium bicarbonate yields highly microporous materials, with BET surface areas of up to  $\sim 2200 \text{ m}^2 \text{ g}^{-1}$  [12]. These materials performed in  $\text{H}_2\text{SO}_4$  electrolyte almost as well as benchmark KOH-ACs. In the present study, a new alternative for generating carbon materials from hydrochar with textural properties matching those of optimized KOH-ACs, *i.e.* BET surface areas of ca.  $3000 \text{ m}^2 \text{ g}^{-1}$  and virtually the same pore size distribution, is proposed. It is based on a mixture of potassium oxalate and melamine as activating agent. Importantly, the AC yield of this procedure is 40-46 % vs.  $\sim 23$  % for KOH activation and 33 % for  $\text{HKCO}_3$  activation. The carbons thus synthesized are able to match the performance of KOH-ACs in conventional electrolytes such as  $\text{H}_2\text{SO}_4$  and  $\text{TEABF}_4/\text{AN}$ , and less conventional ones such as  $\text{EMImTFSI}/\text{AN}$ .

## 2. Experimental section

### 2.1. Synthesis of hydrochar materials

The hydrochar material was prepared by the hydrothermal carbonization (HTC) of eucalyptus sawdust. Briefly, an aqueous dispersion of the raw material (320 g L<sup>-1</sup>) was placed in a Teflon-lined stainless steel autoclave, heated up to 250 °C and kept at this temperature for 4 h. The resulting carbonaceous solid (hydrochar) was recovered by filtration, washed with abundant distilled water and dried at 120 °C over a period of several hours.

### 2.2. Synthesis of porous carbon materials

The hydrochar material was chemically activated using a mixture of potassium oxalate monohydrate (Alfa Aesar) and powdered melamine (Aldrich, 2,4,6-Triamino-1,3,5-triazine). In the first step, the hydrochar material was added to an aqueous dispersion containing potassium oxalate monohydrate ( $K_2C_2O_4$ /hydrochar weight ratio = 2.7, 3.6 and 6) and melamine ( $C_3H_6N_6$ /hydrochar weight ratio in the 0-2 range). Afterwards, the water was evaporated (under magnetic stirring) and the resulting mixture was heat-treated up to 800 °C (heating rate: 3 °C min<sup>-1</sup>) under a nitrogen gas flow and held at this temperature for 1 h (*Note: precautions should be taken when extracting the crucible from the furnace as toxic potassium cyanide is contained in the solid residue*). The samples were then thoroughly washed several times with diluted HCl to remove any inorganic salts (*Note: precautions should be taken when adding HCl as hydrogen cyanide is generated*), then washed with distilled water until neutral pH and finally dried in an oven at 120 °C for 3 h. The activated

carbons thus produced were labeled HCOxK-y-z, where  $y = \text{K}_2\text{C}_2\text{O}_4/\text{hydrochar}$  weight ratio and  $z = \text{C}_3\text{H}_6\text{N}_6/\text{hydrochar}$  weight ratio. The product yield was calculated as the mass of activated carbon/mass of hydrochar  $\times 100$ .

### 2.3. Physical and chemical characterization

Scanning electron microscopy (SEM) images were recorded on a Quanta FEG650 (FEI) instrument, whereas transmission electron microscopy (TEM) images were recorded on a JEOL (JEM 2100-F) apparatus operating at 200 kV. The nitrogen sorption isotherms of the carbon samples were measured at  $-196^\circ\text{C}$  using a Micromeritics ASAP 2020 sorptometer. The apparent surface area ( $S_{\text{BET}}$ ) was calculated from the  $\text{N}_2$  isotherms using the Brunauer-Emmett-Teller (BET) method. An appropriate relative pressure range was selected to ensure a positive line intersect of multipoint BET fitting ( $C > 0$ ) and that the  $V_{\text{ads}}(1 - p/p_0)$  would increase with  $p/p_0$ . [13, 14] The total pore volume ( $V_p$ ) was determined from the amount of nitrogen adsorbed at a relative pressure ( $p/p_0$ ) of  $\sim 0.99$ . The pore size distributions (PSDs) were determined by applying the Quenched-Solid Density Functional Theory (QSDFT) method to the nitrogen adsorption data and assuming a slit pore model. The micropore volume ( $V_{\text{micro}}$ ) was obtained from the QSDFT PSD (pores  $< 2$  nm). Elemental analysis (C, N and O) of the samples was carried out on a LECO CHN-932 microanalyzer. Fourier transform diffuse reflectance infrared spectra (FTIR) of the materials in powder form were recorded using a Nicolet Magna-IR 560 spectrometer fitted with a diffuse reflection attachment. Thermogravimetric analysis (TGA) curves were recorded on a TA Instruments Q6000 TGA system. The Raman spectra were recorded on a Horiba (LabRamHR-800) spectrometer. The source of radiation was a laser operating at a wavelength of 514 nm and at a power of 25 mW. The curve

fitting was performed using a combination of five Gaussian–Lorentzian line shapes that gave the minimum fitting error.

#### 2.4. Electrochemical characterization

The electrodes were composed of 85 wt% of active material, 10 wt% of polytetrafluoroethylene (PTFE) binder (Aldrich, 60 wt% suspension in water) and 5% of Super P (Timcal). The electrochemical measurements were performed in two-electrode Swagelok™ type cells in 1 M H<sub>2</sub>SO<sub>4</sub>, 1 M TEABF<sub>4</sub>/AN (tetraethylammonium tetrafluoroborate/acetonitrile) (≥ 99 %, Sigma-Aldrich), and EMIMTFSI/AN (1-Ethyl-3-methylimidazolium bis(trifluoromethylsulfonyl)imide, weight ratio 1:1) (99 %, Ionic Liquids Technology, Germany) electrolyte solutions. In the case of the H<sub>2</sub>SO<sub>4</sub>- and TEABF<sub>4</sub>/AN-based supercapacitors, the supercapacitors were assembled using two carbon electrodes of comparable mass (carbon loading of 8-10 mg cm<sup>-2</sup>), electrically isolated by a glassy fibrous separator. In the case of the EMIMTFSI/AN-based supercapacitor, mass balancing was performed in order to increase the stability at 3 V (mass positive electrode = 1.1 × mass negative electrode, average mass loading ca. 8 mg cm<sup>-2</sup>). The electrochemical characterization was performed at room temperature using a computer-controlled potentiostat (Biologic VMP3 multichannel generator) and consisted of cyclic voltammetry experiments (CV), and galvanostatic charge/discharge (CD) cycling tests.

Cyclic voltammetry experiments were conducted using a cell voltage of 1 V in 1 M H<sub>2</sub>SO<sub>4</sub>, 2.7 V in 1 M TEABF<sub>4</sub>/AN, and 3 V in EMIMTFSI/AN, at increasing sweep rates from 1 mV s<sup>-1</sup> to 200 mV s<sup>-1</sup>. Plots of cell specific capacitance vs. voltage were calculated using the formula:

$$C_{\text{cell}} = \frac{I}{\nu \cdot m} \quad (2)$$

where  $I$  = current (A),  $\nu$  = scan rate ( $V s^{-1}$ ) and  $m$  = mass (grams) of carbon material in the supercapacitor.

Galvanostatic charge/discharge cycling was carried out using a cell voltage of 1 V in 1 M  $H_2SO_4$ , 2.7 V in 1 M TEABF<sub>4</sub>/AN, and 3 V in EMIMTFSI/AN, at increasing current densities from 0.1 to 100 A g<sup>-1</sup>, based on the active mass of one electrode. The specific gravimetric capacitance of the supercapacitor was determined from the galvanostatic cycles by means of the formula:

$$C_{\text{cell}} = \frac{I}{(dV/dt) \cdot m} \quad (2)$$

where  $dV/dt$  = the slope of the discharge curve ( $V s^{-1}$ ). As most supercapacitors are operated in the range of  $V_{\text{max}}$  to approximately  $\frac{1}{2} V_{\text{max}}$ , the upper half of the discharge curve was used to determine the slope of the discharge curve [15].

To trace the Ragone plots, the specific energy (Wh kg<sup>-1</sup>) and power (kW kg<sup>-1</sup>) were calculated using the following formulae:

$$E = \frac{1}{2} C_{\text{cell}} \Delta V_d^2 \quad (3)$$

$$P = \frac{E}{\Delta t_d} \quad (4)$$

where  $\Delta V_d$  is the operation voltage ( $V_{\text{max}} - IR_{\text{drop}}$ ) and  $\Delta t_d$  is the discharge time.

To calculate the specific volumetric capacitance, and volumetric energy and power densities, the packing density of the electrode was used. This density was determined from its thickness (measured with a micrometer caliper) and its area (0.785 cm<sup>2</sup>) [16].

Long-term cycling stability was evaluated by continuous galvanostatic charge/discharge cycling over 10000 cycles at  $5 \text{ A g}^{-1}$  and at the maximum cell voltage, *i.e.* 1 V in  $\text{H}_2\text{SO}_4$ , 2.7 V in  $\text{TEABF}_4/\text{AN}$  and 3 V in  $\text{EMIImTFSI}/\text{AN}$ . Afterwards, the self-discharge and leakage current were evaluated by constant load tests which consisted in charging at  $1 \text{ A g}^{-1}$  up to the maximum cell voltage, which was then kept stable for 2 h. This was followed by a period of 50 hours at open circuit during which the dependence of cell voltage on time was recorded.

### **3. Results and Discussion**

#### **3.1. Chemical and structural characteristics of the porous carbons**

The morphology of the activated carbons produced by means of the chemical activation of sawdust-derived hydrochar with a mixture of potassium oxalate ( $\text{K}_2\text{C}_2\text{O}_4$ ) and melamine ( $\text{C}_3\text{H}_6\text{N}_6$ ) was examined by SEM. It can be seen from Figure 1a that, regardless of the preparation conditions, the activated particles retain the morphology typical of the sawdust-derived hydrochar, *i.e.* a mixture of fibers and microspherules on their surface (similar results are obtained when potassium oxalate is used by itself, as shown in Figure S1 in Supporting Information) [17]. This contrasts with the results obtained for the samples activated with potassium hydroxide. In this case, the morphology of the original particles is completely transformed during the activation step [18, 19]. The retention of the original morphology after activation constitutes a potential advantage over the use of KOH (similarly to potassium bicarbonate and potassium bicarbonate+melamine [12]), especially when the morphology is an advantageous one such as that of being spherical or nanosheet-like. Closer

inspection of the particles *via* high-resolution transmission electron microscopy (HRTEM) shows a porosity made up of randomly distributed pores, which is typical of activated carbons (Figure 1b). The amorphous-like structure of the activated materials is evidenced by XRD and Raman spectroscopy. Thus, Figure 1c shows XRD patterns with broad and low-intensity (002) and (10) diffraction lines, where the graphene stacking has disappeared completely in the material with the largest proportion of porosity (*i.e.*, HCOxK-3.6-2). Meanwhile, Figure 1d reveals broad, overlapping and similar intensity D ( $\sim 1346\text{ cm}^{-1}$ ) and G ( $\sim 1590\text{ cm}^{-1}$ ) bands in the first order Raman spectra. The ratio of integrated intensities  $I_D/I_G$ , which is used to measure the degree of disorder in carbon materials, has a value of 1.44 and 1.45 for HCOxK-2.7-2 and HCOxK-3.6-2 respectively. These results are similar to those obtained for other hydrochar materials activated with KOH [20, 21] or a mixture of KOH and melamine [18], and other kinds of ACs [10, 11, 22]. In spite of their amorphous nature, these materials possess relatively good electronic conductivities of the order of  $\sim 2\text{-}3\text{ S cm}^{-1}$  (measured at 7 MPa), which is beneficial for electrochemical applications.

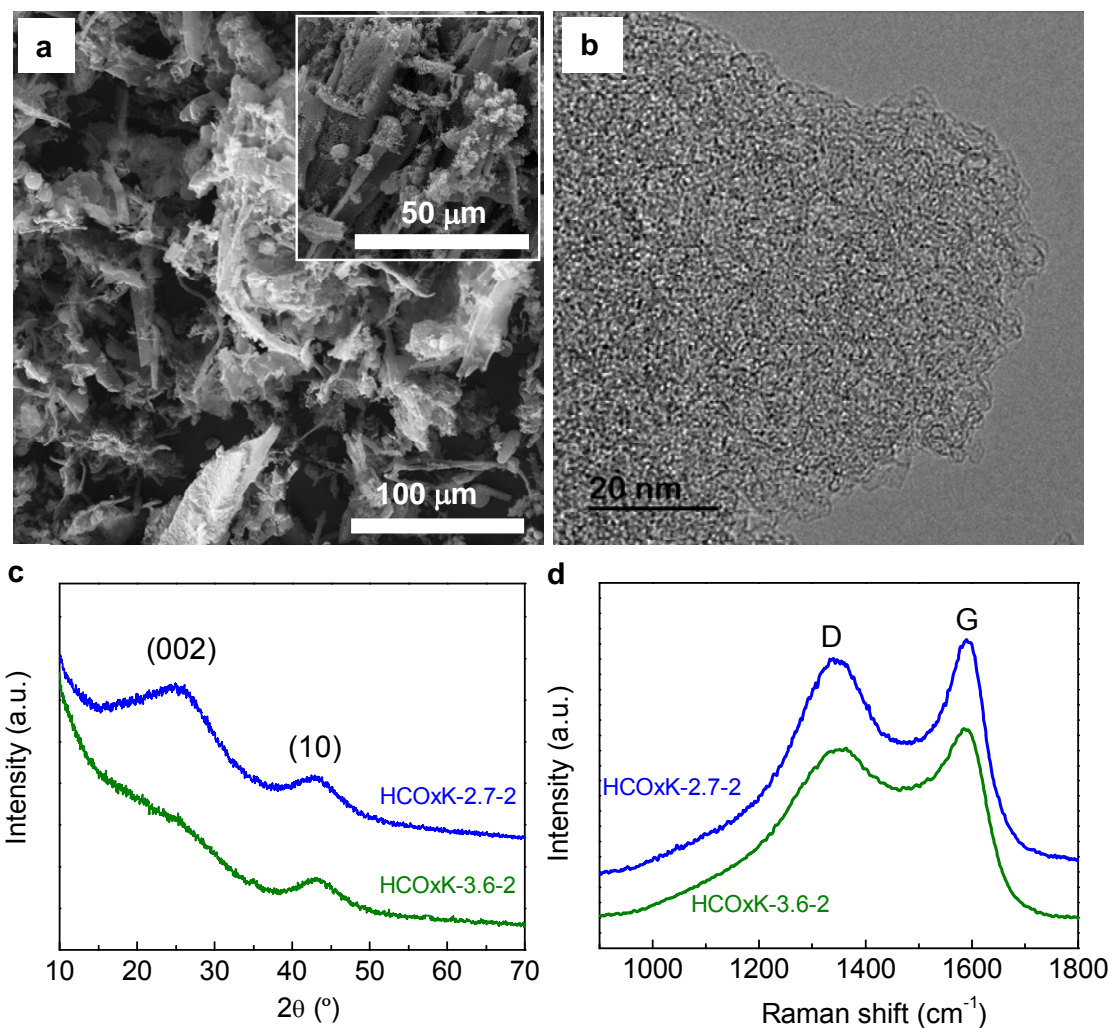


**Figure 1.** a) SEM image of HCOxK-3.6-2 (inset: SEM image of the hydrochar precursor), b) HRTEM image of HCOxK-3.6-2, c) XRD patterns and d) Raman spectra of HCOxK-2.7-2 and HCOxK-3.6-2.

The effect of the preparation conditions on the textural properties of the synthesized activated carbons was studied by  $N_2$  physisorption. As can be seen in Figure 2a, an increase in the melamine/hydrochar ratio causes a marked increment in the amount of  $N_2$  adsorbed and an enlargement of pore size. This is confirmed by the pore size distributions (PSDs) in Figure 2b, which show an increase in size for both pore systems. On the other hand, for a fixed melamine/hydrochar ratio, the increase in the  $K_2C_2O_4$ /hydrochar ratio enhances the amount of  $N_2$  adsorbed and also enlarges the pore size (Figure 2c-d), which

is consistent with the harshening of the activation conditions. These materials are highly microporous, with the micropore volume comprising more than 70 % of the total pore volume (see Table 1). These results differ markedly with those previously achieved by activating hydrochar with KOH [18, 19] or  $\text{KHCO}_3$  [12] in the presence of melamine, which gave rise to materials with a well-balanced micro-mesoporosity ( $V_{\text{microp}}/V_{\text{mesop}} \sim 0.8-1$ ). In the present study, we observe that the activation with  $\text{K}_2\text{C}_2\text{O}_4$  in the presence of melamine does enhance the porosity development (Figure 2a and Table 1) and enlarge the pore size (Figure 2b) compared to the sole use of  $\text{K}_2\text{C}_2\text{O}_4$ , but most of the porosity is kept in the micropore range ( $< 2$  nm). A summary of the textural properties of the porous carbons is presented in Table 1. When  $\text{K}_2\text{C}_2\text{O}_4$  is used as activating agent in the absence of melamine (carbonization temperature = 800-850 °C), the porous carbons are characterized by BET surface areas of 1300-1600  $\text{m}^2 \text{g}^{-1}$  and pore volumes  $< 0.7 \text{ g cm}^{-3}$ , with around 90 % of the pore volume corresponding to micropores. However, when melamine is present, the BET surface area of the materials is  $> 1800 \text{ m}^2 \text{g}^{-1}$  and even approaches 3000  $\text{m}^2 \text{g}^{-1}$  in optimized activation conditions (*i.e.*,  $\text{K}_2\text{C}_2\text{O}_4/\text{hydrochar} = 3.6-6$  and  $\text{melamine}/\text{hydrochar} = 2$ ), while the pore volume increases up to  $1.6 \text{ cm}^3 \text{g}^{-1}$ . Importantly, the textural parameters of these porous carbons show values similar to those obtained under harsh KOH activation conditions [18, 23], with the advantage that potassium oxalate is much less corrosive, the corrosiveness of KOH being one of its main drawbacks for its industrial implementation. In addition, a larger activated carbon yield is obtained, as shown in Table 1. Thus, 40-46 g of activated carbon is produced from 100 g of hydrochar vs.  $\sim 23$  g of activated carbon per 100 g hydrochar for KOH. This means that a much smaller amount

of activating agent and precursor needs to be used to produce the same amount of highly porous carbon, thereby providing both economic and environmental benefits.

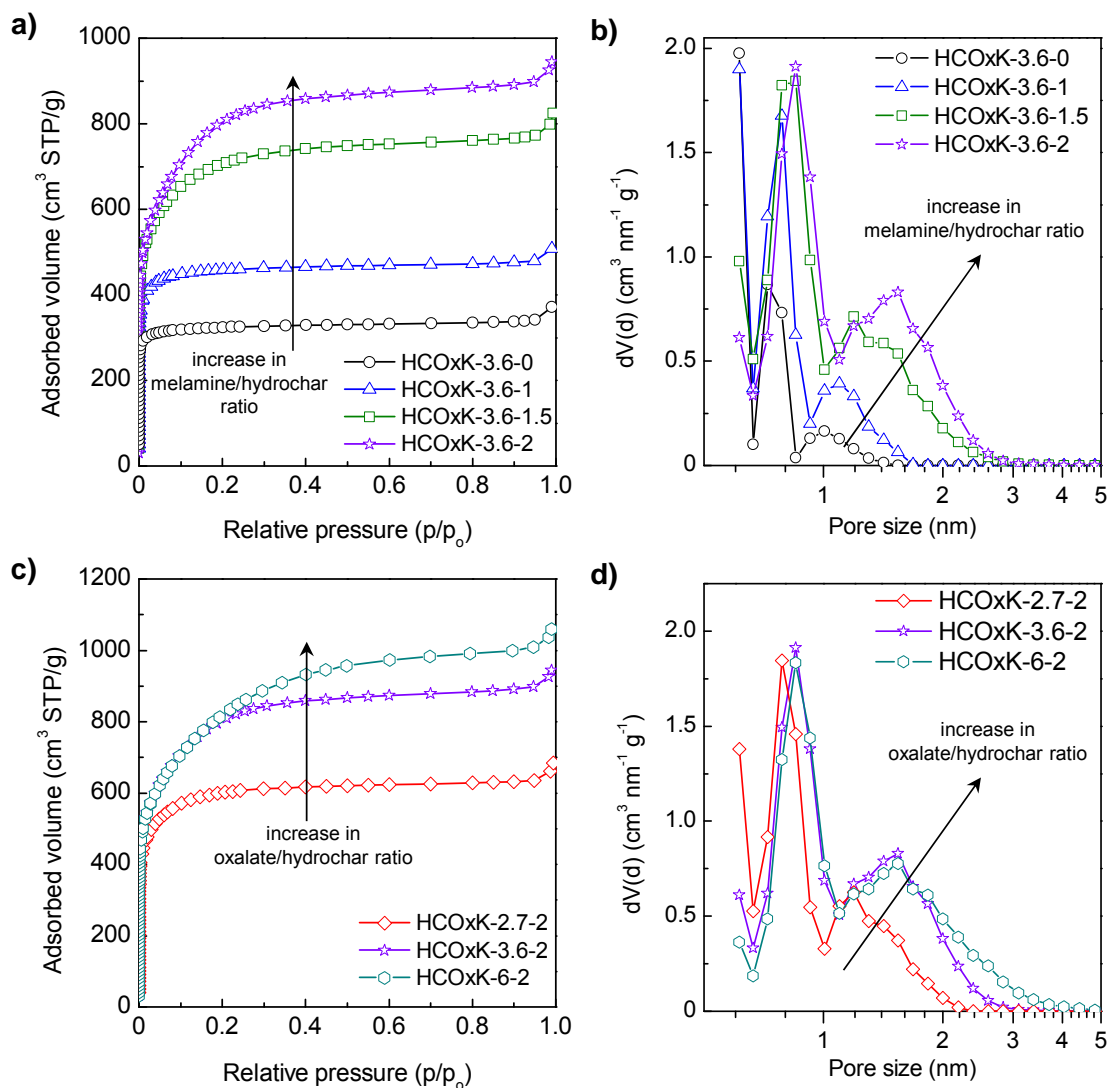


**Figure 2.** N<sub>2</sub> sorption isotherms (a and c) and pore size distributions (b and d) of the porous carbon materials fabricated by using potassium oxalate or a mixture potassium oxalate/melamine as activating agent.

**Table 1.** Textural properties of the porous carbon materials.

Material	Ratio hydrochar/K <sub>2</sub> C <sub>2</sub> O <sub>4</sub> /melamine	T (°C)	Yield (%)	Textural properties			Electrode packing density (g cm <sup>-3</sup> )
				S <sub>BET</sub> [m <sup>2</sup> g <sup>-1</sup> ]	V <sub>p</sub> [cm <sup>3</sup> g <sup>-1</sup> ] <sup>a</sup>	V <sub>micro</sub> [cm <sup>3</sup> g <sup>-1</sup> ] <sup>b</sup>	
HCOxK-3.6-0	1 / 3.6 / 0	800	52	1310	0.57	0.50 (88)	n.d.
		850	48	1600	0.71	0.63 (89)	0.65
HCOxK-3.6-1	1 / 3.6 / 1	800	53	1830	0.78	0.72 (92)	n.d.
HCOxK-3.6-1.5	1 / 3.6 / 1.5	800	46	2640	1.27	1.04 (82)	0.47
HCOxK-3.6-2	1 / 3.6 / 2	800	41	2950	1.46	1.18 (81)	0.43
HCOxK-2.7-2	1 / 2.7 / 2	800	46	2300	1.02	0.89 (87)	0.54
HCOxK-6-1	1 / 6 / 1	800	47	2120	0.93	0.83 (89)	n.d.
HCOxK-6-2	1 / 6 / 2	800	40	2960	1.60	1.14 (71)	n.d.

<sup>a</sup> Total pore volume at P/P<sub>0</sub> ~ 0.99. <sup>b</sup> Micropore volume determined from the QSDFT PSD (pores < 2 nm). The percentage of the total pore volume which corresponds to micropores is indicated in parenthesis.

Similarly to other melamine-mediated chemical activation processes (*v.g.* KOH and HKCO<sub>3</sub>) [12, 18, 19], the activated carbons prepared with potassium oxalate contain a certain amount of nitrogen. As determined by elemental chemical analysis, the bulk nitrogen content of the activated carbons is in the 0.5-0.9 wt.% range, irrespective of the amount of melamine that is added (Table S1).

### 3.2. Mechanism of formation of the porous carbons

The formation of the porous carbons by chemical activation with a mixture of potassium oxalate and melamine was investigated by thermogravimetric analysis of the mixture hydrochar/potassium oxalate/melamine = 1 / 3.6 / 2 (weight) and by X-ray diffraction (XRD), infrared spectroscopy (IR) and elemental analysis (EA) studies of the aforementioned mixture carbonized in a furnace at temperatures in the 500-800 °C range. Figure 3a compares the variations in weight with temperature for potassium oxalate monohydrate, sawdust-based hydrochar and the mixture under study. The TGA curve of potassium oxalate monohydrate shows a first weight loss at

around 110 °C, which corresponds to the loss of hydration water ( $\text{K}_2\text{C}_2\text{O}_4 \cdot \text{H}_2\text{O} \rightarrow \text{K}_2\text{C}_2\text{O}_4 + \text{H}_2\text{O}$ , 10 % weight loss). Then, it decomposes over the range of 500-600 °C according to the reaction:  $\text{K}_2\text{C}_2\text{O}_4 \rightarrow \text{K}_2\text{CO}_3 + \text{CO}$  (~ 15 % weight loss), without yielding any carbon (carbon yield is ca. 0.02 % at 800 °C, following the reaction:  $2 \text{K}_2\text{C}_2\text{O}_4 \rightarrow 2 \text{K}_2\text{CO}_3 + \text{C} + \text{CO}_2$ ), unlike some other organic salts [24]. Meanwhile, carbonization of hydrochar takes place over a wide range of temperatures from 200 °C to 700-800 °C (with a maximum at ~ 380°C on the DTG curve, data not shown). In the case of the hydrochar/potassium oxalate/melamine mixture, the TGA curve shows three sharp weight loss steps in the ranges of 210-310 °C, 520-580 °C and above 700 °C. The first sharp weight loss at 210-310 °C is ascribed to the sublimation of melamine [25-27] and the partial decomposition of  $\text{K}_2\text{C}_2\text{O}_4$  into  $\text{K}_2\text{CO}_3$  and KCN (see XRD discussion below and Figure 3b). Interestingly, the presence of melamine increases the amount of carbonaceous residue considerably. Thus, the product yield for a sample prepared at 400 °C in the presence of melamine is 95 %, compared to only 70 % when activation is carried out with just potassium oxalate (Table S2). This increase in product yield can be attributed to the formation of an amorphous, poorly polymerized carbon nitride from melamine (*vide infra*). This substance decomposes gradually, as shown by the TGA analysis of the sample prepared at 400 °C in the presence of melamine (Figure S2), unlike g- $\text{C}_3\text{N}_4$ , which experiences a sudden weight loss at around 650 °C, as previously reported for a mixture of potassium gluconate and melamine [27] or GO and melamine [26]. The gradual weight loss from 310 to 500 °C is attributed to the pyrolysis of hydrochar and the decomposition of the poorly polymerized carbon nitride, whereas the following sharp weight loss in

the 520-580 °C range corresponds to the main decomposition of oxalate into carbonate, as in the case of potassium oxalate. The final sharp weight loss above 700 °C is ascribed to the following redox reaction [28, 29]:  $\text{K}_2\text{CO}_3 + 2 \text{C} \rightarrow 2 \text{K} + 3 \text{CO}$ . Decomposition of oxygen groups at that temperature also takes place, as evidenced by the decrease in the oxygen content of the material (Table S2).

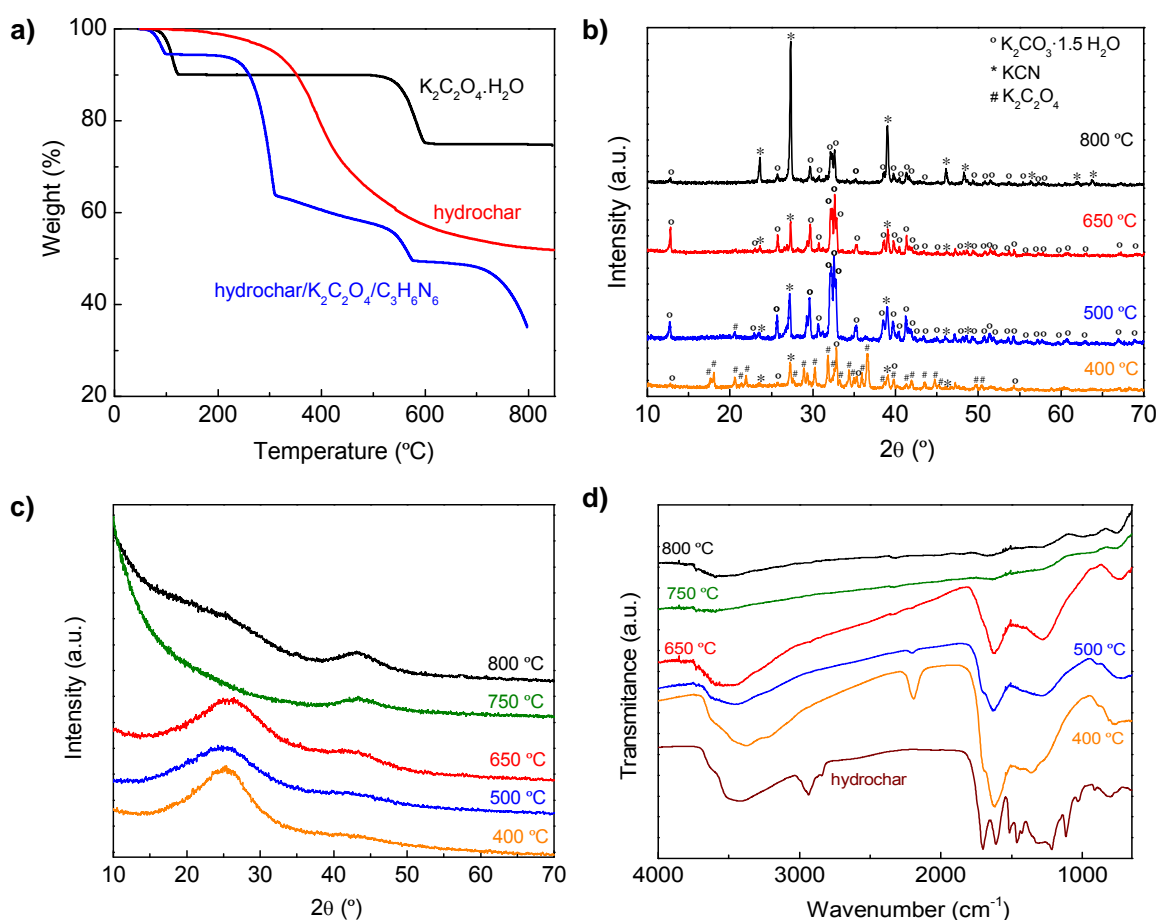


**Figure 3.** a) TGA of monohydrate potassium oxalate, sawdust-derived hydrochar and the mixture hydrochar/potassium oxalate/melamine = 1 / 3.6 / 2, b) XRD patterns of the mixture hydrochar/potassium oxalate/melamine = 1 / 3.6 / 2 carbonized at different temperatures before acid leaching, c) XRD patterns of the mixture hydrochar/potassium oxalate/melamine = 1 / 3.6 / 2 carbonized at different temperatures after acid leaching and d) FTIR spectra of the mixture hydrochar/potassium oxalate/melamine = 1 / 3.6 / 2 carbonized at different temperatures after acid leaching.

Figure 3b shows the XRD patterns of the materials produced as the temperature increases from 400 to 800 °C before acid leaching. At 400 °C, in addition to peaks attributable to  $K_2C_2O_4$ , peaks corresponding to hydrated potassium carbonate appear, showing the partial decomposition of  $K_2C_2O_4$  into  $K_2CO_3$  (which hydrates in contact with air) already at 400 °C, together with peaks ascribable to KCN. Therefore, the decomposition of melamine promotes the partial decomposition of  $K_2C_2O_4$ , generating  $K_2CO_3$  and KCN. This is confirmed by the activation of hydrochar with solely  $K_2C_2O_4$  at 400 °C, which only shows peaks for  $K_2C_2O_4$  (see Figure S3a), and even at 500 °C, which still exhibits intense peaks for  $K_2C_2O_4$ , in addition to  $K_2CO_3$  (see Figure S3b). For  $T \geq 750$  °C, peaks associated to  $K_2CO_3$  are still visible, revealing the presence of un-reacted  $K_2CO_3$ . After acid washing, hydrated potassium carbonate and potassium cyanide are readily dissolved, as proved by the XRD patterns in Figure 3c. For  $T \leq 650$  °C, the XRD patterns show a broad, mid-intensity band at around 25-26°, which can be attributed to poorly polymerized carbon nitride [30]. For  $T \geq 750$  °C, no (002) band attributable to carbon nitride or turbostratic carbon is visible, suggesting no graphene stacking in the walls of the pores of these highly porous materials (Table S2), while the band (10) indicative of the size of the graphene sheets along the basal plane increases slightly from 750 to 800 °C.

The chemical structure of the carbonaceous materials activated at temperatures in the 400-800°C range was analyzed by IR spectroscopy and EA. Figure 3d shows the corresponding FTIR spectra, including for comparison purposes the spectrum of the hydrochar material used as precursor. For  $T \geq 400$  °C, the aliphatic structures which give rise to peaks in the 2800-3000  $cm^{-1}$

region in the hydrochar material disappear. Overall, the H/C ratio decreases from *ca.* 0.07 in the hydrochar material to 0.042 at  $T = 400\text{ }^{\circ}\text{C}$  and to only 0.003 at  $T = 800\text{ }^{\circ}\text{C}$  (see Table S2), the remaining hydrogen being associated to aromatic structures ( $740\text{-}890\text{ cm}^{-1}$ ) and oxygen and nitrogen groups. Similarly, C=O ( $1710\text{ cm}^{-1}$ ) and C-OH moieties ( $\sim 3500$  and  $1110\text{ cm}^{-1}$ ) are gradually eliminated with the increase in temperature, the O/C ratio decreasing from around 0.26-0.28 at  $400\text{-}650\text{ }^{\circ}\text{C}$  to 0.04 at  $800\text{ }^{\circ}\text{C}$  (Table S2). The most prominent feature for  $T \geq 400\text{ }^{\circ}\text{C}$  is the aromatic carbon at  $1620\text{ cm}^{-1}$ . In addition, for the samples activated at  $400$  and  $500\text{ }^{\circ}\text{C}$ , a sharp peak appears at *ca.*  $2200\text{ cm}^{-1}$ , and then completely disappears at  $T \geq 750\text{ }^{\circ}\text{C}$ . This peak, which is attributable to diimides ( $-\text{N}=\text{C}=\text{N}-$ ) and cyanides ( $\text{C}\equiv\text{N}$ ) and is absent in  $\text{g-C}_3\text{N}_4$  [31-34], confirms the presence of poorly polymerized carbon nitride. As can be seen in Table S2, with the rise in the activation temperature, the percentage of N progressively decreases, with the N/C ratio decreasing from  $\sim 0.23$  at  $400\text{ }^{\circ}\text{C}$  to 0.01 at  $T \geq 750\text{ }^{\circ}\text{C}$ . One of the largest nitrogen drops takes place between  $400$  and  $500\text{ }^{\circ}\text{C}$  (Table S2), in agreement with a drastic reduction in intensity of the peak at *ca.*  $2200\text{ cm}^{-1}$ , reflecting the partial decomposition of the carbon nitride formed.

The development of porosity with the increase in activation temperature was followed by  $\text{N}_2$  physisorption. The isotherms and PSDs are shown in Figure 4, whereas the textural properties are listed in Table S2. As can be seen, there is substantial pore development already at  $500\text{ }^{\circ}\text{C}$  ( $S_{\text{BET}} = 980\text{ m}^2\text{ g}^{-1}$ ,  $V_p = 0.43\text{ g/cm}^3$ ), the temperature at which there is a large decrease in nitrogen content (*vide supra*). It is especially worth noting that the development of porosity is much higher than that achieved when using only  $\text{K}_2\text{C}_2\text{O}_4$ . These results appear

to confirm the important role in porosity development played by the decomposition of the carbon nitride (*vide supra*). At 650 °C, the material already possesses a BET surface area and pore volume higher than those achieved at 800 °C using  $K_2C_2O_4$  (see Tables S2 and Table 1). A further increase in temperature to 750 °C, the temperature at which the redox reaction between  $K_2CO_3$  and C takes place (*vide supra*), promotes a large porosity development and an increase in pore size, as reflected by the widening of the knee isotherm (see Figure 4a) and the PSD (see Figure 4b). This trend is accompanied by a 22 % decrease in product yield (Table S2). As this reaction progresses at 800 °C, a slight widening of the PSD is further recorded in parallel with a slight decrease in product yield (*i.e.*, 3 %). It is worth noting that materials with large BET surface areas and pore volumes are already obtained at 650-750 °C (Table S2), and that they also contain an appreciable amount of nitrogen (*i.e.*, 4.4 wt% at 650 °C and 1.2 wt% at 750 °C), which could be advantageous for adsorption-based applications [35-37].

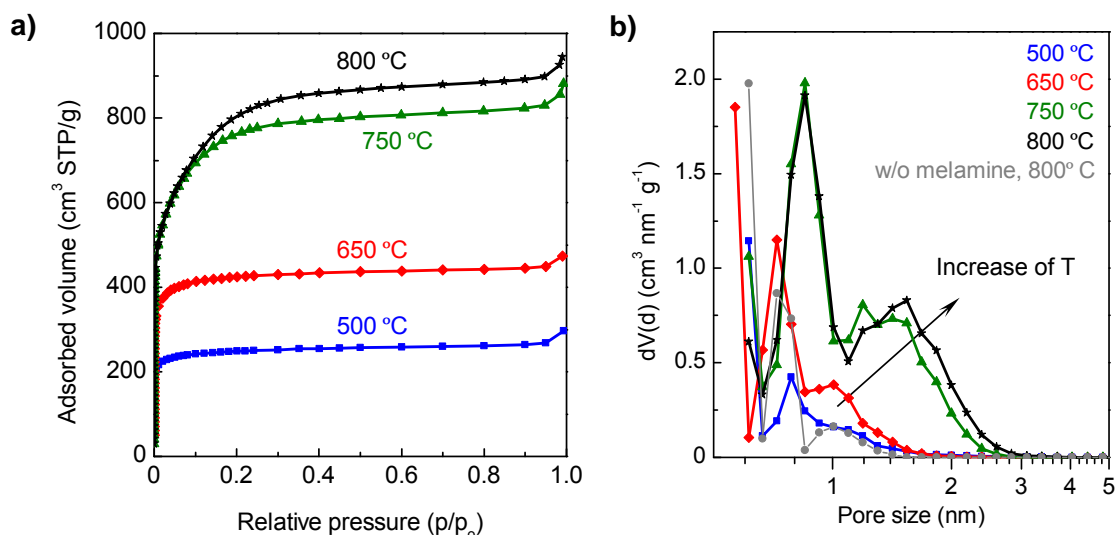


**Figure 4.** a) N<sub>2</sub> sorption isotherms and b) pore size distributions of the mixture hydrochar/potassium oxalate/melamine = 1 / 3.6 / 2 carbonized at different temperatures after acid leaching.

### 3.3. Supercapacitor performance of the porous carbons

In order to confirm the potential of the porous carbons developed, their performance as supercapacitor electrodes was evaluated in conventional electrolytes, such as 1 M H<sub>2</sub>SO<sub>4</sub> and 1 M TEABF<sub>4</sub>/AN, and less conventional ones like EMImTFSI/AN. Figure S4 shows CV curves of the supercapacitors assembled with the porous carbons in the different electrolytes. As can be seen, these materials behave as double-layer capacitors, retaining the characteristic square-shaped voltammogram at rates as high as 200 mV s<sup>-1</sup> regardless of the electrolyte used. The galvanostatic charge/discharge cycles in Figure S5 further confirm their good electrochemical performance, with symmetric voltage profiles at both low and high rates and coulombic efficiencies of 97-100 %. Furthermore, low IR drops are identified at the beginning of the discharge curve at high rates in all the electrolytes (Figures S5b, S5d and S5f), which suggests a good rate capability. This is confirmed by Figures 4a-c, which show the impact of the discharge current on the cell specific capacitance in the different electrolytes (*note that the cell specific capacitance is ¼ of the electrode specific capacitance for symmetric systems, see experimental section for calculations*). In general, therefore, the supercapacitors can work at discharge currents of ≥ 50 A g<sup>-1</sup> with a capacitance retention of > 60 %. The observed differences in rate capability for the different materials correlate well with their PSDs, while the values of gravimetric specific capacitance at low rates follow the trend of surface area (although the surface area-normalized capacitance is slightly enhanced with the narrowing of the PSD, *i.e.* HCOxK-2.7-2 > HCOxK-3.6-1.5 > HCOxK-3.6-2). Thereby, HCOxK-3.6-2 is the material that exhibits the largest gravimetric specific capacitance and also the best rate capability, regardless of the

electrolyte used. On the other hand, as exemplified by Figure 5a, the behavior of HCOxK-3.6-2 matches that of a hydrochar-based KOH activated carbon obtained in optimized conditions (*i.e.*, KOH/hydrochar weight ratio = 4) [12], as both materials possess similar textural properties. Furthermore, the electrochemical performance of all the oxalate/melamine-based ACs surpasses that of the AC specifically developed for supercapacitor applications (see Figures 5a-b). As can be appreciated from Tables S3-S4, the specific capacitance of the supercapacitors based on the porous carbons developed in this work compares very well with that of state-of-the-art porous carbon materials in all the electrolytes used.

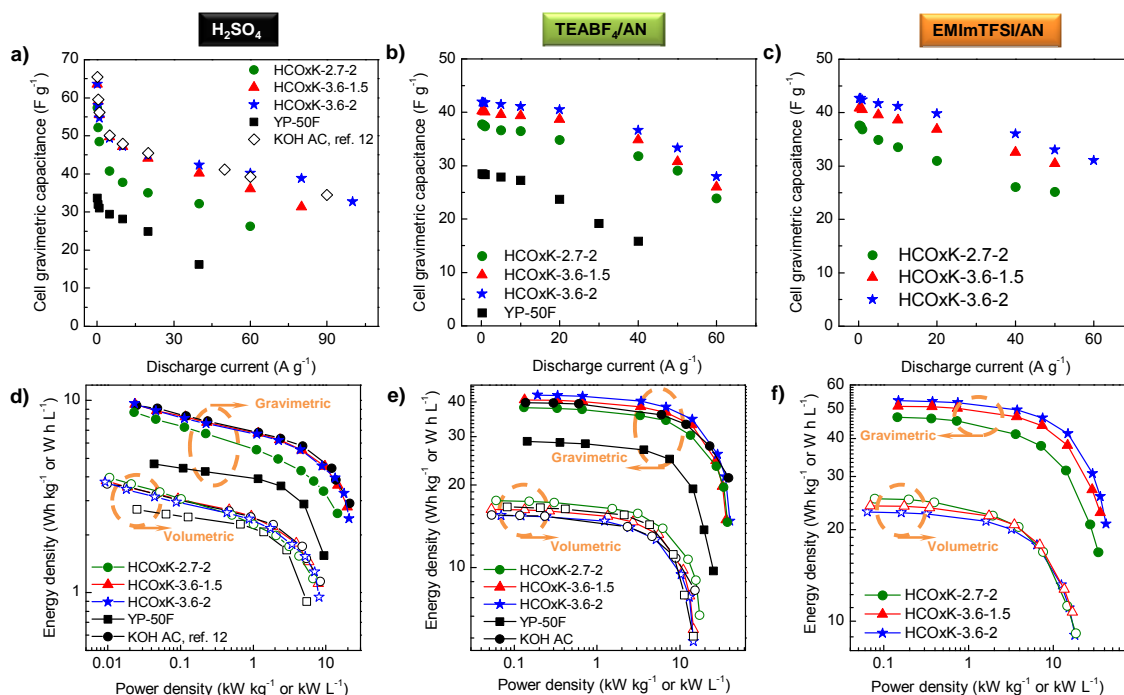


**Figure 5.** Impact of the discharge current on the cell specific capacitance in 1 M H<sub>2</sub>SO<sub>4</sub> (a), 1 M TEABF<sub>4</sub>/AN (b) and EMImTFSI/AN (c) electrolytes, and Ragone-like plots in 1 M H<sub>2</sub>SO<sub>4</sub> (d), 1 M TEABF<sub>4</sub>/AN (e) and EMImTFSI/AN (f) electrolytes.

Figures 5d, 5e and 5f show the Ragone-like plots on both a gravimetric and volumetric basis for the different porous carbons. On a volumetric basis, the performance of the oxalate/melamine-based ACs is quite similar, although on gravimetric basis the carbons with the largest pore developments (BET surface area  $> 2600 \text{ m}^2 \text{ g}^{-1}$ ) exhibit the best energy/power characteristics. The Ragone-like plots further confirm the similar performances of the KOH AC and oxalate/melamine ACs with similar porous textures, and their superior performance when compared to the commercial AC (Figures 5d-e).

Last but not least to be evaluated are the cycling stability, and leakage current and self-discharge of the supercapacitor for its long-term use respectively under charge/discharge conditions or for back-up functions. Figure 6 shows the corresponding results for one of the optimized materials, *i.e.* HCOxK-3.6-1.5 (similar results were obtained for the rest of the carbons). As can be appreciated from Figure 6a, a capacitance retention as high as 98 % is recorded in  $\text{H}_2\text{SO}_4$  (1 V), and a similarly high value of 90 % in the  $\text{TEABF}_4/\text{AN}$  (2.7 V) and EMImTFSI/AN (3 V) electrolytes after 10000 cycles at  $5 \text{ A g}^{-1}$ . These values are similar to those of many carbon materials [38-42], including KOH activated carbons [12, 18, 19, 43-45], and below the limits established by the manufacturers for the end-of-life of the supercapacitor (*i.e.* 20 % capacitance fading) [46], indicating a good stability. On the other hand, leakage currents of  $\sim 5, 8$  and  $15 \text{ mA g}^{-1}$  were recorded after 2 h of constant loading at maximum cell voltage in  $\text{H}_2\text{SO}_4$  (Figure 6b),  $\text{TEABF}_4/\text{AN}$  (Figure 6c) and EMImTFSI/AN (Figure 6d) respectively. As can be seen in Figures 6b, 6c and 6d, the supercapacitor undergoes a quick self-discharge process during the first 2 h after voltage floating in the aqueous electrolyte and during the first 8 h in the

organic electrolytes, thereafter slowing down. The voltage drops to half its value after more than 2 days in  $\text{H}_2\text{SO}_4$  (Figure 6b) and after 16-19 h in the organic electrolytes (Figures 6c-d). These data are in the range of values reported for other carbon-based supercapacitors, such as those based on templated mesoporous carbons [47], highly porous KOH-activated carbons [48], prototype packed cells [49], micro/mesoporous carbon nanosheets [43] and graphene materials [50-52].

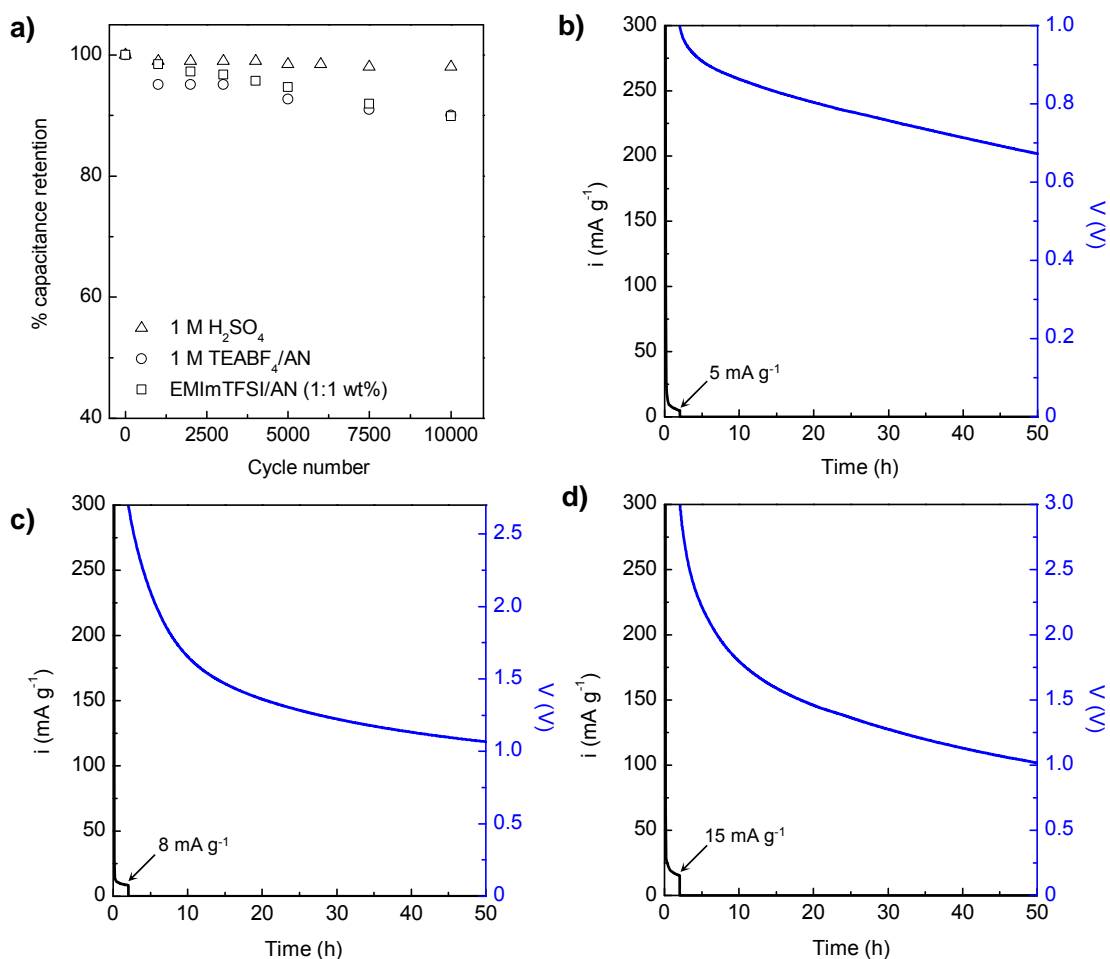


**Figure 6.** Long-term cycling stability studies (10000 cycles,  $5 \text{ A g}^{-1}$ ) in the different electrolytes analyzed (a), and leakage current and self-discharge analyses in 1 M  $\text{H}_2\text{SO}_4$  (b), 1 M  $\text{TEABF}_4/\text{AN}$  (c) and EMImTFSI/AN (d) electrolytes. Material: HCOxK-3.6-2.

#### 4. Conclusions

In summary, highly microporous carbons with textural properties matching those of benchmark KOH activated carbons have been developed by activating hydrochar with a less corrosive activating agent, *i.e.* a mixture composed of potassium oxalate and melamine. Importantly, the product yield of such activation process is approximately double that of the KOH activation process. Melamine is shown to play a key role in the development of porosity. Thus, materials produced by using just potassium oxalate have BET surface areas of 1300-1600 m<sup>2</sup> g<sup>-1</sup> and pore volumes of < 0.7 g cm<sup>-3</sup>. Whereas when melamine is present, the BET surface area of the materials is in the 1800-3000 m<sup>2</sup> g<sup>-1</sup> range and the pore volume increases up to 1.6 cm<sup>3</sup> g<sup>-1</sup>. Furthermore, the micropore size distribution can be tuned by increasing the activation temperature and controlling the ratio hydrochar/potassium oxalate/melamine. These textural characteristics are complemented by a relatively good electronic conductivity, *i.e.*, ~2-3 S cm<sup>-1</sup>. As a result, these materials exhibit a good capacitive performance in aqueous and organic electrolytes, matching that of KOH activated carbons and surpassing that of commercial activated carbons specifically developed for supercapacitors.

#### Acknowledgments

This research work was supported by the FICYT Regional Project (GRUPIN14-102) and Spanish MINECO/FEDER (CTQ2015-63552-R). G. A. F. thanks the MINECO for his predoctoral contract.

## References

- [1] Patrick JW. Porosity in carbons: characterization and applications. London: Edward Arnold; 1995.
- [2] Cooney DO. Activated charcoal : antidotal and other medical uses / David O. Cooney. New York: M. Dekker; 1980.
- [3] Bandosz TJ. Activated carbon surfaces in environmental remediation. Amsterdam: Amsterdam, etc. : Elsevier, Academic Press; 2006.
- [4] Sevilla M, Mokaya R. Energy storage applications of activated carbons: supercapacitors and hydrogen storage. *Energy Environ Sci* 2014;7(4):1250-80.
- [5] Wei L, Yushin G. Nanostructured activated carbons from natural precursors for electrical double layer capacitors. *Nano Energy* 2012;1(4):552-65.
- [6] Wang J, Kaskel S. KOH activation of carbon-based materials for energy storage. *J Mater Chem* 2012;22(45):23710-25.
- [7] Fehler N, Fellingner T-P, Antonietti M. "Salt Templating": A Simple and Sustainable Pathway toward Highly Porous Functional Carbons from Ionic Liquids. *Adv Mater* 2013;25(1):75-9.
- [8] Pampel J, Fellingner TP. Opening of Bottleneck Pores for the Improvement of Nitrogen Doped Carbon Electrocatalysts. *Adv Energy Mater* 2016;6(8):8.
- [9] Pampel J, Denton C, Fellingner T-P. Glucose derived ionothermal carbons with tailor-made porosity. *Carbon* 2016;107:288-96.
- [10] Zhu S, Li J, He C, Zhao N, Liu E, Shi C, et al. Soluble salt self-assembly-assisted synthesis of three-dimensional hierarchical porous carbon networks for supercapacitors. *J Mater Chem A* 2015;3(44):22266-73.
- [11] Deng J, Xiong T, Xu F, Li M, Han C, Gong Y, et al. Inspired by bread leavening: one-pot synthesis of hierarchically porous carbon for supercapacitors. *Green Chemistry* 2015;17(7):4053-60.
- [12] Sevilla M, Fuertes AB. A Green Approach to High-Performance Supercapacitor Electrodes: The Chemical Activation of Hydrochar with Potassium Bicarbonate. *ChemSusChem* 2016;9(14):1880-8.
- [13] ISO 9277:2010. Determination of the specific surface area of solids by gas adsorption - BET method. Second Edition of ISO 9277, ISO. Geneva; 2012.
- [14] Rouquerol F, Rouquerol J, Sing K. Adsorption by powders and porous solids: principles, methodology and applications. San Diego Academic Press; 1999.
- [15] Stoller MD, Ruoff RS. Best practice methods for determining an electrode material's performance for ultracapacitors. *Energy Environ Sci* 2010;3(9):1294-301.
- [16] Fuertes AB, Ferrero GA, Sevilla M. Commentary: Methods of calculating the volumetric performance of a supercapacitor. *Energy Storage Materials* 2016;4:154-5.
- [17] Sevilla M, Antonio Macia-Agullo J, Fuertes AB. Hydrothermal carbonization of biomass as a route for the sequestration of CO<sub>2</sub>: Chemical and structural properties of the carbonized products. *Biomass Bioenerg* 2011;35(7):3152-9.
- [18] Fuertes AB, Sevilla M. High-surface area carbons from renewable sources with a bimodal micro-mesoporosity for high-performance ionic liquid-based supercapacitors. *Carbon* 2015;94(0):41-52.
- [19] Fuertes AB, Sevilla M. Superior Capacitive Performance of Hydrochar-Based Porous Carbons in Aqueous Electrolytes. *ChemSusChem* 2015;8(6):1049-57.
- [20] Wei L, Sevilla M, Fuertes AB, Mokaya R, Yushin G. Hydrothermal Carbonization of Abundant Renewable Natural Organic Chemicals for High-Performance Supercapacitor Electrodes. *Adv Energy Mater* 2011;1(3):356-61.
- [21] Coromina HM, Walsh DA, Mokaya R. Biomass-derived activated carbon with simultaneously enhanced CO<sub>2</sub> uptake for both pre and post combustion capture applications. *J Mater Chem A* 2016;4(1):280-9.

- [22] Tian W, Gao Q, Tan Y, Yang K, Zhu L, Yang C, et al. Bio-inspired beehive-like hierarchical nanoporous carbon derived from bamboo-based industrial by-product as a high performance supercapacitor electrode material. *J Mater Chem A* 2015;3(10):5656-64.
- [23] Sevilla M, Fuertes AB. Sustainable porous carbons with a superior performance for CO<sub>2</sub> capture. *Energy Environ Sci* 2011;4(5):1765-71.
- [24] Sevilla M, Fuertes AB. A general and facile synthesis strategy towards highly porous carbons: carbonization of organic salts. *J Mater Chem A* 2013;1(44):13738-41.
- [25] Groenewolt M, Antonietti M. Synthesis of g-C<sub>3</sub>N<sub>4</sub> Nanoparticles in Mesoporous Silica Host Matrices. *Adv Mater* 2005;17(14):1789-92.
- [26] Lin Z, Song M-k, Ding Y, Liu Y, Liu M, Wong C-p. Facile preparation of nitrogen-doped graphene as a metal-free catalyst for oxygen reduction reaction. *Phys Chem Chem Phys* 2012;14(10):3381-7.
- [27] Fuertes AB, Ferrero GA, Sevilla M. One-pot synthesis of microporous carbons highly enriched in nitrogen and their electrochemical performance. *J Mater Chem A* 2014;2(35):14439-48.
- [28] McKee DW. Fundamentals of Catalytic Coal and Carbon Gasification Mechanisms of the alkali metal catalysed gasification of carbon. *Fuel* 1983;62(2):170-5.
- [29] Hayashi Ji, Horikawa T, Takeda I, Muroyama K, Nasir Ani F. Preparing activated carbon from various nutshells by chemical activation with K<sub>2</sub>CO<sub>3</sub>. *Carbon* 2002;40(13):2381-6.
- [30] Li Q, Yang J, Feng D, Wu Z, Wu Q, Park SS, et al. Facile synthesis of porous carbon nitride spheres with hierarchical three-dimensional mesostructures for CO<sub>2</sub> capture. *Nano Res* 2010;3(9):632-42.
- [31] Li J, Cao C, Hao J, Qiu H, Xu Y, Zhu H. Self-assembled one-dimensional carbon nitride architectures. *Diamond and Related Materials* 2006;15(10):1593-600.
- [32] Guo Q, Yang Q, Yi C, Zhu L, Xie Y. Synthesis of carbon nitrides with graphite-like or onion-like lamellar structures via a solvent-free route at low temperatures. *Carbon* 2005;43(7):1386-91.
- [33] Imanaka H, Khare BN, Elsil JE, Bakes ELO, McKay CP, Cruikshank DP, et al. Laboratory experiments of Titan tholin formed in cold plasma at various pressures: implications for nitrogen-containing polycyclic aromatic compounds in Titan haze. *Icarus* 2004;168(2):344-66.
- [34] Rodil SE, Ferrari AC, Robertson J, Muhl S. Infrared spectra of carbon nitride films. *Thin Solid Films* 2002;420-421:122-31.
- [35] Jia YF, Xiao B, Thomas KM. Adsorption of Metal Ions on Nitrogen Surface Functional Groups in Activated Carbons. *Langmuir* 2002;18(2):470-8.
- [36] Nowicki P, Pietrzak R. Effect of amoxidation of activated carbons obtained from sub-bituminous coal on their NO<sub>2</sub> sorption capacity under dry conditions. *Chemical Engineering Journal* 2011;166(3):1039-43.
- [37] Sun F, Gao J, Liu X, Yang Y, Wu S. Controllable nitrogen introduction into porous carbon with porosity retaining for investigating nitrogen doping effect on SO<sub>2</sub> adsorption. *Chemical Engineering Journal* 2016;290:116-24.
- [38] Puthusseri D, Aravindan V, Madhavi S, Ogale S. 3D micro-porous conducting carbon beehive by single step polymer carbonization for high performance supercapacitors: the magic of in situ porogen formation. *Energy Environ Sci* 2014;7(2):728-35.
- [39] Yu X, Zhao J, Lv R, Liang Q, Zhan C, Bai Y, et al. Facile synthesis of nitrogen-doped carbon nanosheets with hierarchical porosity for high performance supercapacitors and lithium-sulfur batteries. *J Mater Chem A* 2015;3(36):18400-5.
- [40] Hou J, Cao C, Idrees F, Ma X. Hierarchical Porous Nitrogen-Doped Carbon Nanosheets Derived from Silk for Ultrahigh-Capacity Battery Anodes and Supercapacitors. *ACS Nano* 2015;9(3):2556-64.
- [41] Wang H, Zhi L, Liu K, Dang L, Liu Z, Lei Z, et al. Thin-Sheet Carbon Nanomesh with an Excellent Electrocapacitive Performance. *Adv Funct Mater* 2015;25(34):5420-7.

- [42] Xu Y, Lin Z, Zhong X, Huang X, Weiss NO, Huang Y, et al. Holey graphene frameworks for highly efficient capacitive energy storage. *Nat Commun* 2014;5.
- [43] Fuertes AB, Sevilla M. Hierarchical Microporous/Mesoporous Carbon Nanosheets for High-Performance Supercapacitors. *ACS App Mater Interfaces* 2015;7(7):4344-53.
- [44] Kim T, Jung G, Yoo S, Suh KS, Ruoff RS. Activated Graphene-Based Carbons as Supercapacitor Electrodes with Macro- and Mesopores. *ACS Nano* 2013;7(8):6899-905.
- [45] Zhang H, Wang K, Zhang X, Lin H, Sun X, Li C, et al. Self-generating graphene and porous nanocarbon composites for capacitive energy storage. *J Mater Chem A* 2015;3(21):11277-86.
- [46] Maxwell Technologies. "Application note, life duration estimation". <http://www.maxwell.com>
- [47] Fuertes AB, Lota G, Centeno TA, Frackowiak E. Templated mesoporous carbons for supercapacitor application. *Electrochim Acta* 2005;50(14):2799-805.
- [48] Kierzek K, Frackowiak E, Lota G, Gryglewicz G, Machnikowski J. Electrochemical capacitors based on highly porous carbons prepared by KOH activation. *Electrochim Acta* 2004;49(4):515-23.
- [49] Ricketts BW, Ton-That C. Self-discharge of carbon-based supercapacitors with organic electrolytes. *J Power Sources* 2000;89(1):64-9.
- [50] Xu Y, Lin Z, Huang X, Liu Y, Huang Y, Duan X. Flexible Solid-State Supercapacitors Based on Three-Dimensional Graphene Hydrogel Films. *ACS Nano* 2013;7(5):4042-9.
- [51] Xu Y, Chen C-Y, Zhao Z, Lin Z, Lee C, Xu X, et al. Solution Processable Holey Graphene Oxide and Its Derived Macrostructures for High-Performance Supercapacitors. *Nano Letters* 2015;15(7):4605-10.
- [52] El-Kady MF, Kaner RB. Scalable fabrication of high-power graphene micro-supercapacitors for flexible and on-chip energy storage. *Nat Commun* 2013;4:1475.